

High-pressure synthesis and superconductivity of the novel Laves phase BaIr₂

Terunari Koshinuma^{1,2,*}, Hiroki Ninomiya², Izumi Hase², Hiroshi Fujihisa², Yoshito Gotoh², Kenji Kawashima^{2,3}, Shigeyuki Ishida², Yoshiyuki Yoshida², Hiroshi Eisaki², Taichiro Nishio^{1,2}, and Akira Iyo^{2,*}

¹Department of Physics, Graduate School of Science, Tokyo University of Science, Shinjuku, Tokyo 162-8601, Japan

²National Institute of Advanced Industrial Science and Technology (AIST), Tsukuba, Ibaraki 305-8568, Japan

³IMRA JAPAN Co., Ltd., Kariya, Aichi 448-8650, Japan

ABSTRACT

Superconductors comprising 5d transition metals of Ir and Pt have been widely explored because they have the potential of unique superconductivity caused by the strong spin-orbit interaction (SOI). We successfully synthesized BaIr₂, the last Laves phase remaining unsynthesized in the MgCu₂-type AM₂ (A = Ca, Sr, Ba; M = Rh, Pd, Ir, Pt). BaIr₂ was crystallized at 925 °C under a pressure of 3.3 GPa via a solid-state reaction between Ba and Ir powders; it was found to have the longest *a*-lattice constant of 8.038(1) Å among AM₂. BaIr₂ exhibited bulk superconductivity at a transition temperature (*T*_c) of ~2.7 K. BaIr₂ was found to have a type-II superconductor with an upper critical field of 67.7 kOe, which was above the Pauli paramagnetic limit (~50 kOe). The electron–phonon coupling constant and normalized specific heat jump were measured to be 0.63 and 1.2, respectively, indicating that BaIr₂ is a weak-coupling superconductor. The electronic-structure calculations for BaIr₂ revealed that the Ir-5d states are dominant at the Fermi energy (*E*_F) and the density of states at the *E*_F is strongly affected by SOI as in the case of CaIr₂ and SrIr₂.

KEY WORDS

New superconductor, BaIr₂, Laves phase, High-pressure synthesis, Pauli paramagnetic limit, Spin-orbit interaction

* Corresponding authors

E-mail address: koshinuma.terunari@aist.go.jp (T. Koshinuma), iyo-akira@aist.go.jp (A. Iyo).

1. Introduction

In recent years, the search for new superconductors comprising 5d transition metals of Ir and Pt has been actively conducted because of the potential of distinctive superconducting states caused by the strong spin-orbit interaction (SOI) [1-11]. Verifications of unconventional superconductivity in such 5d transition metal-based materials have also been vigorously pursued [12-14].

A Laves phase is a promising target for exploration of such materials, because there are many superconductors composed of 5d transition metals. Among these, MgCu₂-type (C15) CaIr₂ and SrIr₂ Laves phases have been the subject of intensive experimental and theoretical studies [15-20]. In Alr₂, the SOI has been reported to have a significant impact on the physical properties because of the changes in band dispersion, the complexity of the Fermi surface, and enhancement of electron–phonon coupling [15-17,20].

Figure 1 illustrates the crystal structure of the C15 Laves phase (a

cubic system with a space group of *Fd-3m*), and Table 1 summarizes the lattice constants and superconducting transition temperatures (*T*_c) of AM₂ (A = Ca, Sr, Ba; M = Rh, Pd, Ir, Pt) reported thus far, including BaIr₂ synthesized in this study [21].

Superconductivity has been reported only for AM₂ (M = Rh, Ir), and prior to our study, AM₂ had a higher *T*_c with increasing atomic number of A for each M. Gutowska *et al.* performed phonon calculations on SrM₂ (M = Ir, Rh) and reported that the higher the mass of the constituent elements in AM₂, the stronger the electron–phonon coupling. In other words, if BaIr₂ can be synthesized, a *T*_c higher than those of other AM₂ compounds can be expected. However, there were no experimental reports on BaIr₂, which motivated us to synthesize BaIr₂. The synthesis of BaIr₂ is also significant from the viewpoint of inorganic synthetic chemistry.

AM₂ can be regarded as a structure in which atom A is inserted in

the space of a pyrochlore lattice formed by M atoms. $BaIr_2$ does not crystallize under ambient pressure, possibly because of the size of Ba, which is too large to be in the tolerance range wherein the Laves phase is formed.

To crystallize $BaIr_2$ by reducing the size mismatch, herein, we utilize a high-pressure (HP) synthesis method. As a result, we succeeded in synthesizing $BaIr_2$, the C15 Laves phase, and confirmed its superconductivity. This study reports the synthesis, physical-property measurements, and electronic-structure calculation of $BaIr_2$.

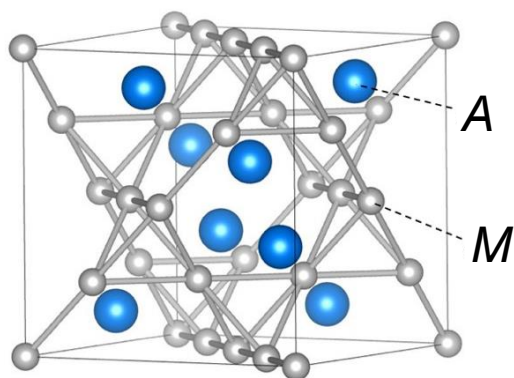


Fig. 1 Schematic of the crystal structure of the $MgCu_2$ -type Laves phase AM_2 (created using VESTA software [22]). Solid lines indicate the unit cell.

Table 1

Lattice constants and T_c of AM_2 ($A = Ca, Sr, Ba$; $M = Pd, Rh, Pt, Ir$).

No superconductivity has been reported in AM_2 ($M = Pd, Pt$).

	Ca	Sr	Ba
Pd	7.665(5) Å [23]	7.826(5) Å [23]	7.953(5) Å [23]
Pt	7.629(5) Å [23]	7.777(5) Å [23]	7.920(5) Å [23]
Rh	7.5326(6) Å 5.13 K [24]	7.72090(5) Å 5.4 K [25]	7.87163(7) Å 5.6 K [25]
Ir	7.545 Å [23] 5.8 K [16]	7.7075(2) Å 5.9 K [17]	8.038(1) Å 2.7 K (This study)

2. Materials and method

2.1 Sample Preparation

Polycrystalline samples were obtained via a solid-state reaction using a cubic-anvil-type HP apparatus (Oh!sawa system, CAP-035) [26]. A Ba ingot (99%, Rare Metallic Co., Ltd.) and Ir powder (99.9%, Rare Metallic Co., Ltd.) were used as starting materials. The Ba ingot

was filed to form a powder. The Ba and Ir powders were weighed and mixed using a mortar in a glove box filled with N_2 gas. Ba in the sample decreased due to diffusion of Ba from the sample to the BN vessel during heating. To compensate for the decrease in Ba, excess Ba (5-20 mol%) was added to the starting composition. Note that metal vessels such as gold could not be used because they react with Ba. In addition, we focused on mixing the large grain-sized Ba powder ($\sim 100 \mu m$) with the fine Ir powder ($\sim 10 \mu m$) as uniformly as possible.

The mixed powder was pressed into a pellet and placed in a BN reaction vessel. The sample was heated for 30 min at a temperature of $\sim 925 \text{ }^\circ C$ under a pressure of 3.3 GPa. $BaIr_2$ was formed at 1.9 GPa and not at 1.0 GPa, indicating that $BaIr_2$ was indeed a HP phase.

The superconductivity (transition width and volume fraction) and yield of $BaIr_2$ in the samples were strongly dependent on the excess Ba and synthesis temperature. When the synthesis temperature was low (e.g., $850 \text{ }^\circ C$) or the excess Ba was too large, samples with poor superconductivity were obtained, although the yield of $BaIr_2$ in the samples was sufficiently high. It was also found that when the synthesis temperature was high (e.g., $1100 \text{ }^\circ C$), samples with good superconductivity in terms of T_c and transition width were obtained, but the ratio of impurity phases was relatively high. In other words, there is a trade-off between phase purity and superconductivity in polycrystalline samples, and the best balance sample was obtained at intermediate temperatures between low and high temperatures (e.g., $900 \text{ }^\circ C$) with a small amount of Ba added to the synthesis. This implies that the superconductivity in $BaIr_2$ is sensitive to off-stoichiometry, as in the case of the Laves phase $LuIr_2$ [27].

The measurements conducted in this study were performed on a sample synthesized at $925 \text{ }^\circ C$ with 6% excess Ba. Because $BaIr_2$ reacted with O_2 and CO_2 in the air and eventually decomposed into $BaCO_3$ and Ir, the samples were treated in a glove box.

2.2 Physical-Property Measurements

Powder X-ray diffraction (XRD) patterns were recorded using a diffractometer (Rigaku, Ultima IV) with $CuK\alpha$ radiation (1.5418 \AA) at room temperature ($\sim 293 \text{ K}$). Measurements were performed using an airtight attachment that prevented the sample from being exposed to air. Rietveld fitting and simulations were performed using the RIETAN-2000 [28].

Magnetization (M) was measured in magnetic fields (H) using a magnetic-property measurement system (Quantum Design, MPMS-

XL7). Temperature (T), dependence of electrical resistivity (ρ), and specific heat (C) were measured using a physical-property measurement system (Quantum Design, PPMS). The composition of the samples was analyzed using an energy dispersive X-ray spectrometer (Oxford, SwiftED3000) attached to an electron microscope (Hitachi High-Technologies, TM-3000).

2.3 Electronic-Structure Calculation

The electronic structure of BaIr_2 was obtained by first-principles calculations using the full-potential linearized augmented plane wave method based on the density functional theory. The WIEN2K [29] computer program was used to conduct the entire calculation. The exchange-correlation potential was approximated using the generalized gradient approximation [30]. We used muffin-tin spheres with radii $r(\text{Ba}) = r(\text{Ir}) = 2.5$ a.u. Plane-wave cutoff K_{max} was chosen such that $R_{\text{mt}} * K_{\text{max}} = 7.0$, where $R_{\text{mt}} = r(\text{Ba}) = r(\text{Ir})$ is the radius of the smallest muffin-tin sphere. We used 1,000 and 8,000 k-points for the self-consistent field and electronic density of states (DOS) calculations. The lattice constant a_{opt} was optimized to minimize the total energy and was found to be equal to 7.902 Å, which is lower than the experimental value presented later. The SOI was included in the calculations using a second variational approach.

3. Results and discussion

3.1 XRD Measurement

Figures 2(a) and 2(b) show the powder XRD pattern of the sample and the simulated diffraction pattern of the BaIr_2 Laves phase. They are in good agreement with each other, except for the small diffraction peaks associated with Ir and other unknown substances. Upon comparing both the XRD patterns in more detail, it was found that the relative intensity of the observed (220) peak was higher than that of the simulated (220) peak, possibly because the diffraction peak associated with the unknown substances overlaps with the (220) peak. The molar composition ratio Ba:Ir of the sample was measured to be 0.97(3):2.00(2). Based on the above experimental results, we concluded that BaIr_2 was obtained as the main phase in the sample.

We evaluated the lattice constant of BaIr_2 and the molar ratio of BaIr_2 and Ir in the sample using Rietveld fitting. The a -axis length of BaIr_2 was determined to be 8.038(1) Å (atomic coordinates (x, y, z) of Ir and Ba are (0, 0, 0) and (3/8, 3/8, 3/8), respectively), which is the longest among those for AM_2 listed in Table 1. The crystallization

of BaIr_2 was possibly realized because Ba ions shrink to a greater extent than the pyrochlore lattice under HP, resulting in a tolerance range suitable for the formation of the Laves phase. The longest a -axis length may support the above-mentioned crystallization mechanism for BaIr_2 . The BaIr_2 :Ir molar ratio in the sample was estimated to be 0.81:0.19; this result was used to analyze the specific heat.

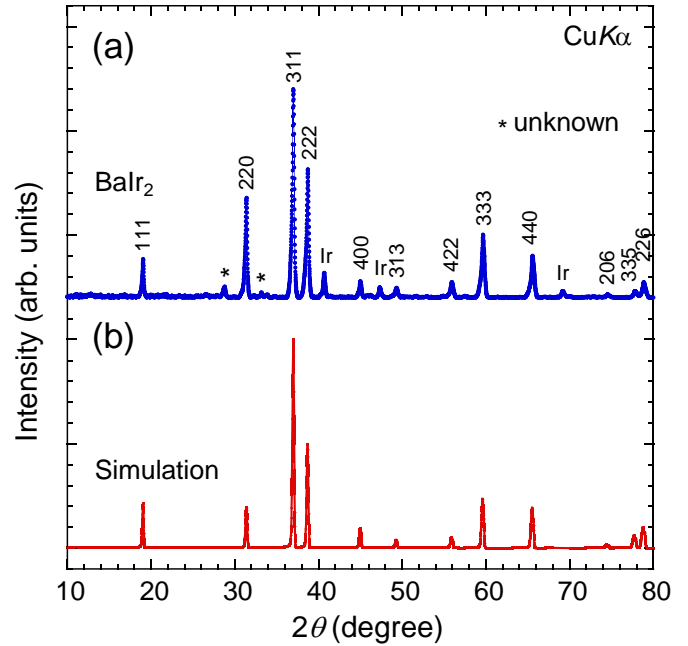


Fig. 2(a) Powder XRD pattern of the sample synthesized under HP. Background noise is eliminated from the data. The peaks corresponding to BaIr_2 are labeled with diffraction indices. (b) Simulated XRD pattern of the BaIr_2 assuming the MgCu_2 -type structure.

3.2 Superconducting Properties

Figure 3 shows the T dependence of $4\pi M/H$ for the sample. The experimental data were demagnetization field corrected using a demagnetization factor N ($=0.15$) estimated from the shape of the measurement sample [31]. A pronounced diamagnetic transition due to the occurrence of superconductivity was observed at a T_c of ~ 2.7 K. The zero-field-cooling (ZFC) magnetization at 2 K is 85% of the full shielding diamagnetism ($4\pi M/H = -1$), which was large enough as bulk superconductivity. Because Ir does not exhibit superconductivity above 2 K [32], the observed superconductivity was attributed to BaIr_2 . The T_c of BaIr_2 was approximately half those of CaIr_2 and SrIr_2 , which is not in accordance with the theoretical prediction [15].

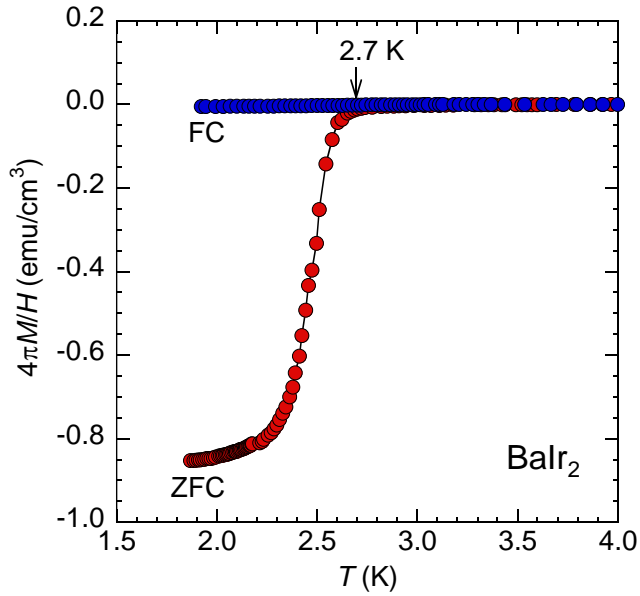


Fig. 3 T dependence of $4\pi M/H$ for the sample. Measurements were performed with ZFC and field-cooling (FC) modes under a magnetic field of 10 Oe. Demagnetization field correction was performed on M considering the shape of the sample [31].

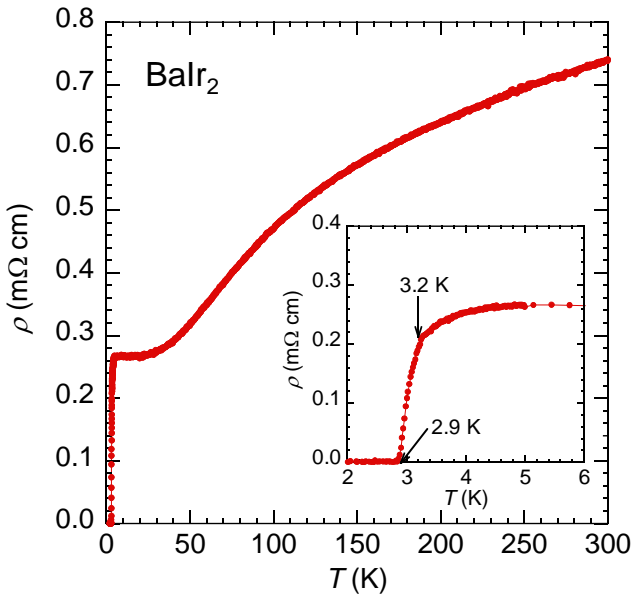


Fig. 4 T dependence of ρ for the sample. The inset shows the enlargement around superconducting transition.

Figure 4 shows the T dependence of ρ below 300 K at $H = 0$ Oe for the sample. The ρ showed metallic T dependence with a residual resistivity ratio, defined as $\rho(300\text{ K})/\rho(5\text{ K})$, of ~ 2.8 . As shown in the inset of Fig. 4, an abrupt decrease in ρ due to superconductivity was observed at ~ 3 K, and the resistance became zero at 2.9 K.

The T dependence of ρ under H of up to 25 kOe for the sample is shown in Figure 5. The parallel shifts of the superconducting

transition in H allowed accurate evaluation of the upper critical field (H_{c2}).

The inset of Fig. 5 shows the T -dependent H_{c2} defined at the midpoint of the superconducting transition curves. $H_{c2}(0)$ is obtained to be 67.7 kOe by the fitting performed with the Ginzburg–Landau (GL) theory [33], $H_{c2}(T) = H_{c2}(0)[(1-(T/T_c)^2)/(1+(T/T_c)^2)]$, where $H_{c2}(0)$ is the upper critical field at 0 K.

The $H_{c2}(0)$ of Balr_2 was found to be higher than those of Calr_2 and SrIr_2 (40–65 kOe [15–17]) despite Balr_2 having a considerably lower T_c . Therefore, the $H_{c2}(0)$ of Balr_2 exceeded the Pauli paramagnetic limit (H_{Pauli}) of $1.86T_c = 50$ kOe [34,35]. The GL coherence length (ξ_0) was calculated to be 69.7 Å using the equation $H_{c2}(0) = \Phi_0/2\pi\xi_0^2$, where Φ_0 is the magnetic flux quantum.

We estimated the orbital limit (H_{orb}) to be 56.2 kOe using $H_{\text{orb}} = 0.698T_c(|dH_{c2}/dT|_{T=T_c})$, where $T_c = 2.94$ K and $|dH_{c2}/dT|_{T=T_c} = 27.4$ kOe/K, based on the Werthamer-Helfand-Hohenberg (WHH) theory [36]. The Maki parameter (α_M), which is defined as $\alpha_M = \sqrt{2}H_{\text{orb}}/H_{\text{Pauli}}$ [37], was calculated to be 1.45. This α_M value is larger than that expected for a typical type-II superconductor ($\alpha_M < 1$), indicating that the paramagnetic pair breaking effect is dominant in Balr_2 .

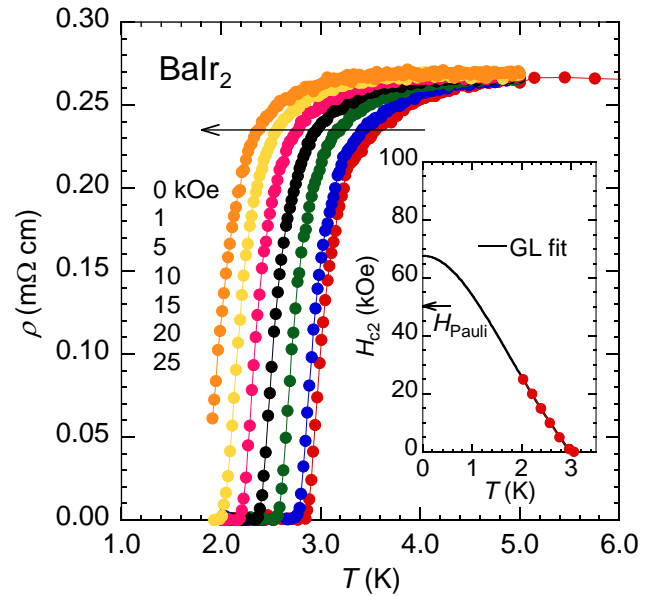


Fig. 5 T dependence of ρ in H of up to 25 kOe for the sample. The inset shows the T dependence of H_{c2} determined at the midpoint of the superconducting transition curves. The solid curve indicates the GL fitting.

Figure 6 shows the H dependence of M for the samples measured at several temperatures below T_c . At $T = 1.9$ K, M showed a broad minimum at ~ 260 Oe. The minimum shifted to a lower H with an

increase in the measured T .

When determining the lower critical field H_{c1} based on the $M-H$ data, it is generally defined by the magnetic field at which the magnetization process begins to deviate from a linear behavior associated with perfect diamagnetism. However, it is probably difficult to determine the H_{c1} accurately when the T_c value is close to the temperature where the $M-H$ data was collected, as in the case of BaIr_2 . Therefore, we defined the H_{c1} by the relation $H_{c1} = H_p/(1-N)$ as reported in the literature [38]. Here, H_p is referred to as the penetration field, which is defined as the intersection point between the extrapolation of perfect diamagnetism and a level of the minimum magnetization, as indicated by the dashed lines in Fig. 6. [39]. Although this method may slightly overestimate the value of H_{c1} , it allows for the systematic evaluation of the H_{c1} at each temperature [40].

As indicated by the solid line in the inset of Fig. 6, the H_{c1} thus obtained was in agreement with that reproduced by the following formula based on the GL theory: $H_{c1}(T) = H_{c1}(0)[1-(T/T_c)^2]$. We calculated $H_{c1}(0)$ to be 286 Oe. The London penetration depth λ_0 of 1520 Å was derived using the equation $H_{c1}(0) = \Phi_0/\pi\lambda_0^2$.

The GL parameter of $\kappa_{\text{GL}} = \lambda_0/\xi_0$ is determined to be 21.8, indicating that BaIr_2 is a type-II superconductor ($\kappa_{\text{GL}} > 1/\sqrt{2}$).

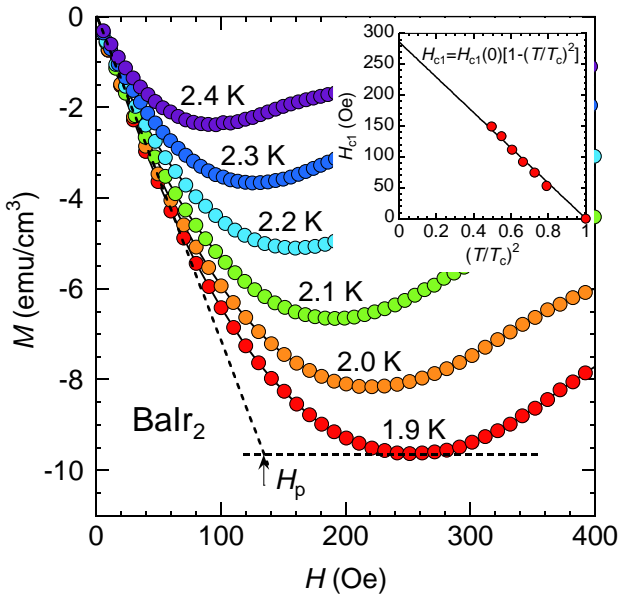


Fig. 6 H dependence of M at several temperatures below T_c for the sample. The inset shows H_{c1} as a function of $(T/T_c)^2$. The solid line indicates a fitting based on the GL theory.

The measurement of C was performed on a sample cut from the same pellet as that used for the powder XRD and magnetization

measurements. The contribution of Ir in the sample to C was subtracted using the reported parameters [31] according to the molar ratio in the sample estimated by Rietveld analysis [41]. The contribution of unknown substances to C was not included in the analysis. However, the amount of the unknown substances in the sample was small judging from the XRD pattern; thus, the impact on the analysis results was considered to be minimal.

The T^2 dependence of C/T for BaIr_2 thus obtained is shown in Figure 7. A clear jump in the specific heat indicates the bulk nature of superconductivity. The data for T^2 in the 7–20 K² range were fitted with $C/T = \gamma_n + \beta T^2$, where γ_n (the Sommerfeld constant) and β are the coefficients associated with the electron and phonon contributions to the total specific heat ($C = C_{\text{el}} + C_{\text{ph}}$), respectively. The fitting yields the values for γ_n and β as 12.0 mJ mol⁻¹ K⁻² and 1.83 mJ mol⁻¹ K⁻⁴, respectively. The Debye temperature Θ_D was calculated to be 147 K using $\beta = (12/5)N\pi R\Theta_D^{-3}$, where $R = 8.314$ J mol⁻¹ K⁻² and $N = 3$ (N is the number of atoms per formula unit cell). The Θ_D of BaIr_2 is lower than that of CaIr_2 and SrIr_2 (160–214 K [15–17]), which can be qualitatively explained as the effect of the larger atomic weight of Ba. The T_c of the sample is as low as 2.7 K, and a good linear fitting is obtained at $T^2 < 20$ K², as shown in Fig 7. Therefore, the obtained values of γ_n and β are expected to be almost the same even if superconductivity is suppressed by applying a magnetic field.

The inset shows the T dependence of C_{el} , which is obtained by subtracting the phonon contribution from C . The thermodynamically determined T_c was 2.35 K. The electron-phonon coupling constant λ_{e-p} in BaIr_2 was evaluated using the McMillan equation [42], $\lambda_{e-p} = (\mu^* \ln(1.45T_c/\Theta_D) - 1.04)(1 - 0.62\mu^*) / (1.04 + \ln(1.45T_c/\Theta_D))$, where μ^* is a Coulomb pseudopotential parameter. Using $T_c = 2.35$ K, $\Theta_D = 147$ K, and the standard μ^* value (0.13), λ_{e-p} was calculated to be 0.63. The λ_{e-p} of BaIr_2 was considerably smaller than that (0.79–1.17) of CaIr_2 and SrIr_2 [15–17]. The normalized specific heat jump ($\Delta C_{\text{el}}/\gamma_n T_c$) was estimated to be ~ 1.2 , which is obtained from the fitting with the α -model [43]. This value is close to that obtained through the Bardeen–Cooper–Schrieffer (BCS) model (1.43). The measured values of λ_{e-p} and $\Delta C_{\text{el}}/\gamma_n T_c$ indicate that BaIr_2 is a weak-coupling superconductor. The values of $\Delta C_{\text{el}}/\gamma_n T_c$ strongly depend on A ($= \text{Ca, Sr, Ba}$) in Alr_2 . These values were reported to be 0.89 for CaIr_2 and 1.71 and 2.08 for SrIr_2 [15–17]. The physical parameters experimentally evaluated for BaIr_2 in this study are listed in Table 2.

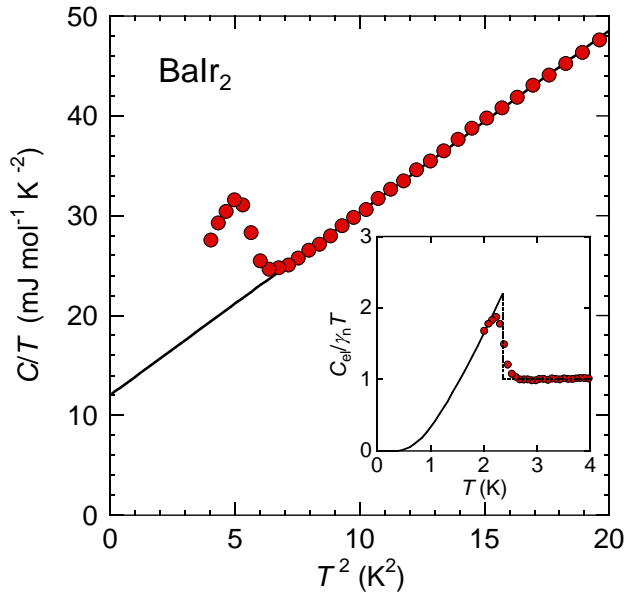


Fig. 7 C/T vs. T^2 for BaIr_2 below 5 K at the zero field. The solid line shows the fitting of data for $T^2 = 7\text{--}20 \text{ K}^2$ with $C/T = \gamma_n + \beta T^2$ and its extrapolation to $T = 0 \text{ K}$. The inset shows the T dependence of $C_{\text{el}}/\gamma_n T$. The solid curve shows the fitting with the α -model.

Table 2

The physical parameters experimentally evaluated for BaIr_2 in this study.

Parameters	Values
a	8.038(1) Å
T_c	2.7 K
$H_{c1}(0)$	286 Oe
$H_{c2}(0)$	67.7 kOe
α_M	1.45
λ_0	1520 Å
ξ_0	69.7 Å
κ_{GL}	21.8
γ_n	12.0 mJ mol ⁻¹ K ⁻²
β	1.83 mJ mol ⁻¹ K ⁻⁴
Θ_D	147 K
λ_{e-p}	0.63
$N(0)$	3.12 states eV ⁻¹ f.u. ⁻¹
$\Delta C_{\text{el}}/\gamma_n T_c$	1.2

3.3 Electronic-Structure Calculation

Figure 8 shows the DOS of BaIr_2 obtained by the first-principles calculations with the SOI. The inset shows the magnification of the total DOS near E_F calculated with and without SOI. As in the cases

of CaIr_2 [16] and SrIr_2 [17], the DOS at the Fermi energy (E_F), $N(0)$, was mostly contributed by the Ir-5d states, and E_F was located at a valley caused by the splitting of the DOS peak due to the strong SOI. The $N(0)^{\text{cal}}$ determined by the calculation with SOI was 3.15 states eV⁻¹ f.u.⁻¹ (f.u. is formula unit), which is in good agreement with the $N(0)$ (3.12 states eV⁻¹ f.u.⁻¹) estimated from the experimentally obtained parameters γ_n and λ_{e-p} using the expression $3\gamma_n = \pi^2 k_B^2 N(0)(1 + \lambda_{e-p})$.

The $N(0)$ of BaIr_2 was comparable to that reported for CaIr_2 and SrIr_2 (3.49 and 2.74 eV⁻¹ f.u.⁻¹, respectively). Therefore, the lower T_c in BaIr_2 , approximately half of that of CaIr_2 and SrIr_2 , cannot be explained by $N(0)$. The lower T_c in BaIr_2 is possibly attributed to weaker electron–phonon interactions.

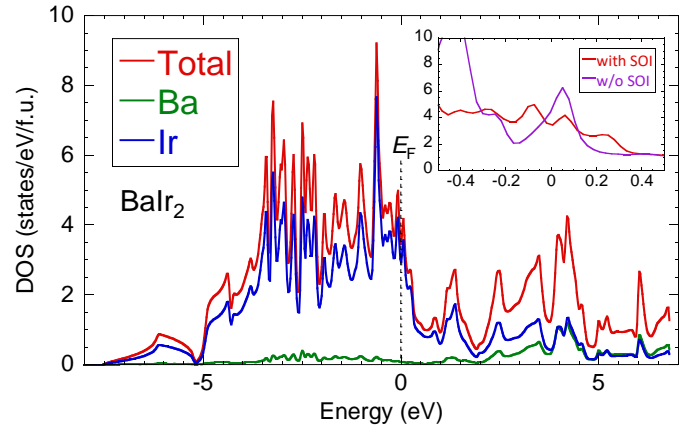


Fig. 8 Total and partial electronic DOS for BaIr_2 obtained by the first-principles calculation with SOI; $E = 0 \text{ eV}$ corresponds to the Fermi energy E_F . The inset is the magnification of the total DOS near the E_F calculated with/without SOI.

4. Conclusion

We successfully synthesized BaIr_2 , a novel C15 Laves phase superconductor, using the HP synthesis technique. BaIr_2 was found to be a type-II superconductor ($T_c = 2.7 \text{ K}$) with a large $H_{c2}(0)$ of 67.7 kOe beyond the Pauli paramagnetic limit. BaIr_2 was classified as a weak-coupling superconductor based on the experimentally determined $\Delta C_{\text{el}}/\gamma_n T_c$ and λ_{e-p} . The band structure calculation confirmed that the effect of the SOI on $N(0)$ in BaIr_2 is strong, similar to that observed in the cases of CaIr_2 and SrIr_2 . In fact, the calculated $N(0)$ with the SOI was in good agreement with the experimentally estimated value. This study also revealed that the superconductivity of BaIr_2 , such as T_c , H_{c2} , and specific heat jump, is significantly different from those of CaIr_2 and SrIr_2 . Further theoretical and experimental studies are needed to elucidate the mechanism

underlying the particularity of BaIr_2 .

ACKNOWLEDGMENTS

This work was supported by JSPS KAKENHI (grant numbers JP19K04481, JP19K03731, and JP19H05823).

References

- [1]. E. Bauer, G. Hilscher, H. Michor, C. Paul, E. W. Scheidt, A. Gribanov, Y. Seropegin, H. Noe, M. Sgrist, and P. Rogl, *Phys. Rev. Lett.* **92**, (2004), 027003. Heavy Fermion Superconductivity and Magnetic Order in Noncentrosymmetric CePt_3Si . <https://doi.org/10.1103/PhysRevLett.92.027003>
- [2]. P. Badica, T. Kondo, K. Togano, *J. Phys. Soc. Jpn.* **74**, (2005), 1014-1019. Superconductivity in a New Pseudo-Binary $\text{Li}_2\text{B}(\text{Pd}_{1-x}\text{Pt}_x)_3$ ($x = 0-1$) Boride System. <https://doi.org/10.1143/JPSJ.74.1014>
- [3]. T. Shibaayama, M. Nohara, H. A. Katori, Y. Okamoto, Z. Hiroi, H. Takagi, *J. Phys. Soc. Jpn.* **76**, (2007), 073708. Superconductivity in Rh_2Ga_9 and Ir_2Ga_9 without Inversion Symmetry. <https://doi.org/10.1143/JPSJ.76.073708>
- [4]. Y. Nishikubo, K. Kudo, M. Nohara, *J. Phys. Soc. Jpn.* **80**, (2011), 055002. Superconductivity in the Honeycomb-Lattice Pnictide SrPtAs . <http://dx.doi.org/10.1143/JPSJ.80.055002>
- [5]. G. Eguchi, D. C. Peets, M. Kriener, Y. Maeno, E. Nishibori, Y. Kumazawa, K. Banno, S. Maki, H. Sawa, *Phys. Rev. B* **83**, (2011), 024512. Crystallographic and superconducting properties of the fully gapped noncentrosymmetric $5d$ -electron superconductors CaMSi_3 ($M = \text{Ir, Pt}$). <https://doi.org/10.1103/PhysRevB.83.024512>
- [6]. T. Takayama, K. Kuwano, D. Hirai, Y. Katsura, A. Yamamoto, H. Takagi, *Phys. Rev. Lett.* **108**, (2012), 237001. Strong Coupling Superconductivity at 8.4 K in an Antiperovskite Phosphide SrPt_3P . <https://doi.org/10.1103/PhysRevLett.108.237001>
- [7]. S. Pyon, K. Kudo, M. Nohara, *J. Phys. Soc. Jpn.* **81**, (2012), 053701. Superconductivity Induced by Bond Breaking in the Triangular Lattice of IrTe_2 , <https://doi.org/10.1143/JPSJ.81.053701>
- [8]. S. Pyon, K. Kudo, J. Matsumura, H. Ishii, G. Matsuo, M. Nohara, H. Hojo, K. Oka, M. Azuma, V. O. Garlea, K. Kodama, S. Shamoto, *J. Phys. Soc. Jpn.* **83**, (2014), 093706. Superconductivity in Noncentrosymmetric Iridium Silicide Li_2IrSi_3 , <http://dx.doi.org/10.7566/JPSJ.83.093706>
- [9]. Y. Okamoto, T. Inohara, Y. Yamakawa, A. Yamakage, K. Takenaka, *J. Phys. Soc. Jpn.* **85**, (2016), 013704. Superconductivity in the Hexagonal Ternary Phosphide ScIrP . <https://doi.org/10.7566/JPSJ.85.013704>
- [10]. K. Horigane, K. Takeuchi, D. Hyakumura, R. Horie, T. Sato, T. Muranaka, K. Kawashima, H. Ishii, Y. Kubozono, S. Orimo, *New J. Phys.* **21**, (2019), 093056. Superconductivity in a new layered triangular-lattice system Li_2IrSi_2 . <https://doi.org/10.1088/1367-2630/ab4159>
- [11]. K. Kudo, H. Hiiragi, T. Honda, K. Fujimura, H. Idei, M. Nohara, *J. Phys. Soc. Jpn.* **89**, (2020), 013701. Superconductivity in $\text{Mg}_2\text{Ir}_3\text{Si}$: A Fully Ordered Laves Phase. <https://doi.org/10.7566/JPSJ.89.013701>
- [12]. E. Bauer, and Manfred Sgrist, eds. Non-centrosymmetric superconductors: introduction and overview. Vol. 847. Springer Science & Business Media, 2012.
- [13]. M. Nishiyama, Y. Inada, and Guo-qing Zheng, *Phys. Rev. Lett.* **98**, (2007), 047002. Spin Triplet Superconducting State due to Broken Inversion Symmetry in $\text{Li}_2\text{Pt}_3\text{B}$, <https://doi.org/10.1103/PhysRevLett.98.047002>
- [14]. P. K. Biswas, H. Luetkens, T. Neupert, T. Stürzer, C. Baines, G. Pascua, A. P. Schnyder, M. H. Fischer, J. Goryo, M. R. Lees, H. Maeter, F. Brückner, H.-H. Klauss, M. Nicklas, P. J. Baker, A. D. Hillier, M. Sgrist, A. Amato, D. Johrendt, *Phys. Rev. B* **87**, (2013), 180503(R). Evidence for superconductivity with broken time-reversal symmetry in locally noncentrosymmetric SrPtAs , <https://doi.org/10.1103/PhysRevB.87.180503>
- [15]. S. Gutowska, K. Górnicka, P. Wójcik, T. Klimczuk, B. Wiendlocha, *Phys. Rev. B* **104**, (2021), 054505. Strong-coupling superconductivity of SrIr_2 and SrRh_2 : Phonon engineering of metallic Ir and Rh. <https://doi.org/10.1103/PhysRevB.104.054505>
- [16]. N. Haldolaarachchige, Q. Gibson, L. M. Schoop, H. Luo, R. J. Cava, *J. Phys.: Condens. Matter* **27**, (2015), 185701.

- Characterization of the heavy metal pyrochlore lattice superconductor CaIr_2 . <https://doi.org/10.1088/0953-8984/27/18/185701>
- [17]. R. Horie, K. Horigane, S. Nishiyama, M. Akimitsu, K. Kobayashi, S. Onari, T. Kambe, Y. Kubozono, J. Akimitsu, *J. Phys.: Condens. Matter* **32**, (2020), 175703. Superconductivity in 5d transition metal Laves phase SrIr_2 . <https://doi.org/10.1088/1361-648X/ab6a2e>
- [18]. X. Yang, H. Li, T. He, T. Taguchi, Y. Wang, H. Goto, R. Eguchi, R. Horie, K. Horigane, K. Kobayashi, J. Akimitsu, H. Ishii, Y. Liao, H. Yamaoka, Y. Kubozono, *J. Phys.: Condens. Matter* **32**, (2020), 025704. Superconducting behavior of a new metal iridate compound, SrIr_2 , under pressure. <https://doi.org/10.1088/1361-648X/ab4605>
- [19]. Y. Zhang, X. M. Tao, M.Q. Tan, *Chinese Phys. B* **26** (2017), 047401. Density-functional theory study on the electronic properties of Laves phase superconductor CaIr_2 . <https://doi.org/10.1088/1674-1056/26/4/047401>
- [20]. H. M. Tütüncü, H. Y. Uzunok, Karaca, E. Arslan, G. P. Srivastava, *Phys. Rev. B* **96**, (2017), 134514. Effects of spin-orbit coupling on the electron-phonon superconductivity in the cubic Laves-phase compounds CaIr_2 and CaRh_2 . <https://doi.org/10.1103/PhysRevB.96.134514>
- [21]. It is mentioned in ref. [18] that the research on superconductivity of BaIr_2 is in progress and a paper is in preparation, but we could not find the corresponding paper.
- [22]. K. Momma, F. Izumi, *J. Appl. Crystallogr.* **41**, (2008), 653-658. VESTA: a three-dimensional visualization system for electronic and structural analysis. <https://doi.org/10.1107/S0021889808012016>
- [23]. E. A. Wood, V. B. Compton, *Acta Crystallogr.* **11**, (1958), 429-433. Laves-phase compounds of alkaline earths and noble metals. <https://doi.org/10.1107/S0365110X58001134>
- [24]. K. Go'rnicka, R. J. Cava, T. Klimczuk, *J. Alloys Compd.* **793**, (2019), 393-399. The electronic characterization of the cubic Laves-phase superconductor CaRh_2 . <https://doi.org/10.1016/j.jallcom.2019.04.199>
- [25]. C. Gong, Q. Wang, S. Wang, H. Lei, *J. Phys.: Condens. Matter* **32**, (2020), 295601. Superconducting properties of MgCu_2 -type Laves phase compounds SrRh_2 and BaRh_2 . <https://doi.org/10.1088/1361-648X/ab7c12>
- [26]. P. M. Shirage, K. Miyazawa, M. Ishikado, K. Kihou, C. H. Lee, N. Takeshita, H. Matsuhata, R. Kumai, Y. Tomioka, T. Kito, H. Eisaki, S. Shamoto, A. Iyo, *Physica C* **469**, (2009), 9. High-pressure synthesis and physical properties of new iron (nickel)-based superconductors. <https://doi.org/10.1016/j.physc.2009.03.027>
- [27]. Y. Takano, H. Takigami, K. Ohhata, K. Sekizawa, *Solid State Commun.* **61**, (1987), 611. Superconductivity in the Lu-Ir alloy system. [https://doi.org/10.1016/0038-1098\(87\)90371-1](https://doi.org/10.1016/0038-1098(87)90371-1)
- [28]. F. Izumi, T. Ikeda, *Materials Science Forum* **321**, (2000), 198-205. A Rietveld-Analysis Programm RIETAN-98 and its Applications to Zeolites. <https://doi.org/10.4028/www.scientific.net/MSF.321-324.198>
- [29]. P. Blaha, K. Schwarz, G. K. H. Madsen, D. Kvasnicka, J. Luitz, WIEN2k, An Augmented Plane Wave + Local Orbitals Program for Calculating Crystal Properties (Vienna: Vienna University of Technology, 2001).
- [30]. J. P. Perdew, K. Burke, M. Ernzerhof, *Phys. Rev. Lett.* **77**, (1996), 3865. Generalized Gradient Approximation Made Simple. <https://doi.org/10.1103/PhysRevLett.77.3865>
- [31]. D. U. Gubser, R. J. Soulen, *J. Low Temp. Phys.* **13**, (1973), 211-226. Thermodynamic properties of superconducting iridium. <https://doi.org/10.1007/BF00654062>
- [32]. R. Prozorov, V. G. Kogan, *Phys. Rev. Applied* **10**, (2018), 014030. Effective Demagnetizing Factors of Diamagnetic Samples of Various Shapes. <https://doi.org/10.1103/PhysRevApplied.10.014030>
- [33]. J. P. Carbotte, *Rev. Mod. Phys.* **62**, (1990), 1027. Properties of boson-exchange superconductors. <https://doi.org/10.1103/RevModPhys.62.1027>
- [34]. A. M. Clogston, *Phys. Rev. Lett.* **9**, (1962), 266. Upper Limit for the Critical Field in Hard Superconductors. <https://doi.org/10.1103/PhysRevLett.9.266>
- [35]. B. S. Chandrasekhar, *Appl. Phys. Lett.* **1**, (1962), 7. A NOTE ON THE MAXIMUM CRITICAL FIELD OF HIGH-FIELD SUPERCONDUCTORS. <https://doi.org/10.1063/1.1777362>
- [36]. N. R. Werthamer, E. Helfand and P. C. Hohenberg, *Phys. Rev.* **147**, (1966) 295. Temperature and Purity Dependence of the Superconducting Critical Field, H_{c2} . III. Electron Spin and Spin-Orbit Effects. <https://doi.org/10.1103/PhysRev.147.295>
- [37]. K. Maki and T. Tsuneto, *Progress of Theoretical Physics* **31**, 6, (1964), 945-956. Pauli Paramagnetism and Superconducting

State. <https://doi.org/10.1143/PTP.31.945>

- [38]. H. Kiessig, U. Essmann, W. Wiethaup, Phys. Lett. A, **71**, (1979), 467-470. Anisotropy of H_{c1} and B_0 in superconducting niobium. [https://doi.org/10.1016/0375-9601\(79\)90638-8](https://doi.org/10.1016/0375-9601(79)90638-8)
- [39]. J. A. Osborn, Phys. Rev. **67**, (1945), 351. Demagnetizing Factors of the General Ellipsoid. <https://doi.org/10.1103/PhysRev.67.351>
- [40]. Y. Tomioka, S. Ishida, M. Nakajima, T. Ito, H. Kito, A. Iyo, H. Eisaki, S. Uchida, Phys. Rev. B **79**, (2009), 132506. Three-dimensional nature of normal and superconducting states in BaNi_2P_2 single crystals with the ThCr_2Si_2 -type structure. <https://doi.org/10.1103/PhysRevB.79.132506>
- [41]. M. Fukuma, K. Kawashima, M. Maruyama, J. Akimitsu, J. Phys. Soc. Jpn. **80**, (2011), 024702. Superconductivity in W_5SiB_2 with the T_2 Phase Structure. <https://doi.org/10.1143/JPSJ.80.024702>
- [42]. W. L. McMillan, Phys. Rev. **167**, 331 (1968). Transition Temperature of Strong-Coupled Superconductors. <https://doi.org/10.1103/PhysRev.167.331>
- [43]. David C Johnston, *Supercond. Sci. Technol.* **26**, (2013), 115011. Elaboration of the α -model derived from the BCS theory of superconductivity. <http://dx.doi.org/10.1088/0953-2048/26/11/115011>

